Solid-State NMR on the Family of Positive Electrode Materials Li_2Ru_1-ySn_yO_3 for Li-ion batteries

Elodie Salager, Vincent Sarou-Kanian, M. Sathiya, Mingxue Tang, Jean-Bernard Leriche, Philippe Melin, Zhongli Wang, Hervé Vezin, Catherine Bessada, Michael Deschamps, et al.

Solid-State NMR on the Family of Positive Electrode Materials $Li_2Ru_{1-y}Sn_yO_3$ for Li-ion batteries

Elodie Salager,[1,2*] Vincent Sarou-Kanian,[1,2] M. Sathiya,[3,4,5] Mingxue Tang[1,2], Jean-Bernard Leriche,[2,4] Philippe Melin,[1,2] Zhongli Wang,[1,2] Hervé Vezin,[6] Catherine Bessada,[1,2] Michael Deschamps[1,2] and Jean-Marie Tarascon[2,3,5]

1. CNRS, CEMHTI (UPR3079), Université d'Orleans, 1D avenue de la recherche scientifique, 45071 Orléans Cedex 2, France
2. Réseau sur le Stockage Electrochimique de l'Energie (RS2E), CNRS FR3459, 33 rue Saint Leu, 80039 Amiens Cedex, France
3. Collège de France, CNRS FRE3357, 11 place Marcelin Berthelot, 75005 Paris, France
4. Laboratoire de Réactivité et de Chimie des Solides (UMR 7314), Université de Picardie Jules Verne, 33 rue Saint Leu, 80039 Amiens Cedex, France
5. Alistore European Research Institute, CNRS FR3104, 33 rue Saint Leu, 80039 Amiens Cedex, France
6. Université Lille Nord de France, CNRS UMR 8516-LASIR, Univ. Lille 1, F-59655 Villeneuve d'Ascq, France

KEYWORDS. Lithium, battery, positive electrode, nuclear magnetic resonance, solid-state NMR, paramagnetic, disorder, Ruthenium, Tin, substitution

ABSTRACT: The possibilities offered by *ex situ and in situ operando* ^{7}Li solid-state nuclear magnetic resonance (NMR) are explored for the $Li_2Ru_{1-y}Sn_yO_3$ family ($0<y<1$), shown previously to display cationic and anionic redox activity when used as a positive electrode for Li-ion batteries. *Ex situ* NMR spectroscopic studies indicate a non-random Sn/Ru substitution in the family. In the first charge an increased metallicity at 4 V is deduced from the NMR spectra. Surprisingly, no striking difference is observed at 4.6 V compared to the pristine electrode, although the electronic structure is expected to be very different and the local cation environment to be distorted. For *in situ operando* measurements we designed a new electrochemical cell that is compatible with NMR spectroscopy and one-dimensional magnetic resonance imaging (MRI). These *operando* measurements validate the *ex situ* observations and indicate that the environment formed at 4 V is specific of the initial charge and that there is little, if not, electrolyte decomposition, even at 4.6 V. This is another attractive feature of these compounds.

Introduction

Layered materials have been instrumental for energy storage in lithium-ion batteries. $LiCoO_2$'s ability to intercalate lithium ions allowed Sony to commercialize batteries based on the rocking-chair principle.[1] Ever since, researchers have been working on ways to improve the properties of this material. Two great advances are worth being recalled. The first one over the 2001-2008 period deals with the partial replacement of Co^{3+} with Ni^{2+} and Mn^{4+}, which has led to the first new version of layered oxides $Li(Ni_{1/3}Mn_{1/3}Co_{1/3})O_2$, coined as NMC.[2,3] These materials turn out to be very attractive since they display higher capacities (~ 200 mAh/g) than the three-dimensional ($LiMn_2O_4$, $LiNi_{0.5}Mn_{1.5}O_4$) spinels (140 mAh/g) or than the most performing polyanionic compound $LiFePO_4$ (170 mAh/g).[4–6] These Li-NMC electrodes are progressively replacing $LiCoO_2$ in today's Li-ion cells. Further explorations of cationic substitutions in the layered oxide systems back to 2001 has led to materials made of Ni, Co, Mn and Li in the metallic layers. In this case, in addition to the Li present in the lithium layer, up to 1/3 of the 3d-metals can be replaced by Li, leading to materials termed Li-rich NMC,[7–9] showing capacities exceeding 280 mAh/g. The origin of this extra capacity has however remained mysterious owing to the complexity of their structure, which can be viewed either as a solid solution of Li_2MO_3 and $LiM'O_2$ or as a composite made of small separate domains of these two phases.[6,10,11]

The processes at stake in Li_2MO_3-type structures have been recently investigated in the families of $Li_2Ru_{1-y}M_yO_3$ materials, with M being Mn[12] and Sn.[13] The $Li_2Ru_{1-y}Sn_yO_3$ material was shown to provide the best capacity retention and the lowest voltage decay of the whole family. These exceptional properties were ascribed to the electrochemically inactive tin atoms that contribute to the stability of the framework during intercalation and deintercalation. The participation of the anionic network to the electrochemical processes, leading to the staggering capacities reported, was also demonstrated. Detailed local structure information to effectively understand the Li-driven motion of cations and anions during cycling is however still missing due to the "transparency" of lithium to many of the experimental techniques used in the previous studies.

It is worth recalling here that the two materials Li_2SnO_3 and Li_2RuO_3 are made of lithium layers sandwiched between LiM_2 layers forming honeycombs (M surrounding Li). They crystallize in the same space group (C2/c) alternating oxygen and cation layers, but they differ in the way the LiM_2 layers are stacked, leading to different superstructure patterns.[14–16] X-ray diffraction studies[13] have demonstrated earlier the existence of a solid solution between the two end-members Li_2SnO_3 and Li_2RuO_3. Nothing is known however about i) the arrangement of the Ru and Sn atoms as they could not be separated in previous X-ray diffraction studies and ii) the arrangement of Li owing to its low electronic density masked by the heavy Ru and Sn atoms.

Li solid-state Nuclear Magnetic Resonance (NMR) spectroscopy is a very sensitive tool to study local structure around the lithium and to follow structural changes in these paramagnetic materials, especially for materials with chemical disorder that cannot be easily characterized by diffraction methods. A ^{7}Li NMR study on Li_2MnO_3,[17] with a similar layered structure, reported that the ^{7}Li NMR signatures were sufficiently different for Li in the Li layers and in the Mn layers to be distinguished. Paik et al. showed that Li was extracted from both layers upon chemical etching.[18] In parallel, $^{6/7}$Li NMR has been used to study NMC and Li-excess NMC, following the pioneering work of Grey et al.[19–22] Li NMR also allowed to study cation ordering in mixed lithium-ruthenium(V) oxides.[23–26] To push the limits further, we explore the possibilities offered by ^{7}Li solid-state NMR in the $Li_2Ru_{1-y}Sn_yO_3$ series. Keeping in mind the complexity of the NMR spectra for paramagnetic systems that are chemically disordered (Ru/Sn substitution), the experiments were designed to combine the advantages of complementary *ex situ* and *operando* measurements. The best resolution in NMR is reached with *ex situ* studies; it necessitates however a series of batteries stopped at various potentials for the characterization and therefore samples sparsely the charge-discharge processes. On the contrary, *in situ* experiments allow studying the battery without the need to open it, and eliminate variations arising from small differences in the various batteries for a better quantification. *Operando* NMR studies go one step further by monitoring the battery in real time, while it is cycling, with a better time and voltage resolution.[27–31] In the case of these highly reactive materials, real-time measurements are precious as they reduce the risk of relaxation of the materials. For *operando* measurements, we designed an electrochemical cell compatible with one-dimensional imaging and used chemical shift imaging to identify the position of the electrolyte giving several sharp signals in the NMR spectrum. The *in situ* broad spectroscopic signature of the electrode is followed during charge and complements the *ex situ* measurements at different potentials.

The experimental results on the structural analysis of the family of $Li_2Ru_{1-y}Sn_yO_3$ pristine materials are reported here together with the solid-state NMR study of the $Li_2Ru_{0.75}Sn_{0.25}O_3$ compound upon cycling, using complementary *ex situ* and *in situ operando* measurements.

Experimental Section

The $Li_2Ru_{1-y}Sn_yO_3$ powders were made as previously described by annealing at high temperatures (900 °C) stoichiometric amounts of RuO_2 (Sigma-Aldrich 99.9%), SnC_2O_4 (Sigma-Aldrich 98%) and 10% excess of Li_2CO_3 (Sigma-Aldrich, 99.0%) to compensate for its volatility at high temperature. Powdered electrodes made of 90% $Li_2Ru_{1-y}Sn_yO_3$ and 10% carbon super P (CSP, Timcal) were cycled in swageloks at a rate C/20 (1 Li per Ru in 20h) and stopped at various states of charge.

For the *ex situ* ^{7}Li NMR study, the pristine materials and the washed electrodes were packed in 1.3 mm outer diameter rotors in an Argon glovebox, closed tightly with

a cap and spun under N_2 using magic angle spinning (MAS). The *ex situ* data reported here were acquired on a 4.7 T Avance III HD Bruker spectrometer (^{7}Li frequency of 77.7 MHz). The ^{7}Li spectra were obtained using a double resonance 1.3 mm Bruker probe with rotors spun at 62.5 kHz (unless mentioned otherwise) and a Hahn-echo sequence synchronized with one rotor period (16 μs). The RF field strength was 170 kHz. The longitudinal relaxation times T_1 were measured for each sample and the recycling delays always allowed full relaxation of the spins, except for the diamagnetic SEI part. The ^{7}Li shifts were referenced to a 1 mol.L^{-1} solution of LiCl at 0 ppm. For paramagnetic compounds the shifts depend on temperature; the values given here were measured with the probe at room temperature, and correspond to a temperature inside the rotor close to 50°C due to frictional heating. The 1D spectra of figure 1 and S1 were fitted with Gaussian lines using the dmfit software.[32] The narrow spectrum of diamagnetic Li_2SnO_3 was acquired differently, on a 17.6 T Avance III Bruker spectrometer using a 2.5 mm Bruker probe, with a spinning rate of 20 kHz for proper fitting of the quadrupolar lineshape. In that case Voigt functions were used. Details of the deconvolution and simulated spectra are given in SI.

In situ ^{7}Li NMR spectra were acquired on a 9.4 T Avance I Bruker spectrometer equipped with a diff50 Bruker probe, with a 50 G/cm/A gradient coil and a Bruker 40 A GREAT40 gradient amplifier. We modified the probe to pass the electrical connections of our new electrochemical cell to the galvanostat in a shielded tube at the centre of the probe body.

The main body of our new electrochemical cell is a 10 mm outer/6 mm inner diameter Kel-f® (polychlorotrifluoroethene) cylinder, a polymer chosen for its excellent hydrophobic and mechanical properties. The current collector on the negative side is a 2 mm-thick Cu disk fitted with a silver-coated Cu wire. On the positive side we used an Al disk with an Al wire. O-rings ensure airtightness at each wire and at the connections of the two main parts of the cell.

The *operando* study was performed on a half battery containing 13.4 mg of a plastic composite electrode (in accordance with Bellcore's plastic Li-ion technology) containing $Li_2Ru_{0.75}Sn_{0.25}O_3$ / CSP / PVDF-HFP in ratios 80/10/10, a Li metal disc (0.3 mm thick) and Whatman GF/D borosilicate glass fibre sheets soaked with a homemade electrolyte (1 mol.L^{-1} $LiPF_6$ in EC/PC/DMC in weight ratio 1:1:3). The electrochemical charge and discharge was controlled by a Biologic VSP galvanostat, using a constant current of 58 μA (one Li per Ru inserted in 30 hours). The spectra were acquired with a α-τ-α-τ-acq echo sequence with an echo delay τ = 12 μs between the excitation pulse and the refocusing pulse. The pulse lengths (5 μs) were chosen to obtain the largest bandwidth available with the highest possible RF field strength of 50 kHz. The recycling delay was voluntarily shortened (250 ms) so as to enhance the signals from the fast-relaxing (paramagnetic) parts, limit the contribution from the free electrolyte and speed up the acquisition. Each spectrum was collected in 29 min (0.02 Li inserted during acquisition) and we acquired 120 spectra in a full charge. Referencing of the shifts is challenging because it is difficult to align perfectly the electrodes with the magnetic center of the magnet. We referenced the *in situ* spectra by setting the most intense peak for the electrolyte at 0 ppm.

The image-spectrum correlations were obtained using a standard spin-echo chemical shift imaging sequence, with 32 scans and a repetition time of 180 ms. The image dimension was acquired with 256 increments and a maximum gradient strength of 379 G/cm (field of view of 16 mm; 62.5 μm between each slice). The acquisition time in the spectroscopic dimension was 9 ms.

The crystal structures obtained by random substitution of Ru by Sn (no partial occupancy) were generated from the Li_2RuO_3 structure with the program supercell by Okhotnikov and Cadars.[33] The substitution was performed using one unit cell (6 Sn/Ru per unit cell). The probability of each type of Li environment was assessed by a careful analysis of these structures.

Results and discussion

a) The pristine materials from an NMR point of view

The ^{7}Li spectra were first collected for all the members of the $Li_2Ru_{1-y}Sn_yO_3$ series (Fig. 1) with the hope to obtain further local structural information on the respective positioning of Ru, Sn and Li in these phases as the amount of Ru changes.

We focus first on the electrochemically inactive and diamagnetic end-member of the solid solution Li_2SnO_3, which is reported as an ionic conductor with poor electronic conductivity.[34] A ^{7}Li NMR spectrum acquired at 17.6 T is shown in Figure 1b. The best fit was obtained with 2 components at shifts of 0.8 ppm (28%), -0.3 ppm (72%). These shifts are in the typical diamagnetic range and confirm the material (electronically) insulating character. This is also supported by the relatively long longitudinal relaxation times (T_1 = 1.46 s). The signals are sharp and indicate good crystallinity, but the intensities do not match exactly those expected (50% and 25% for the two similar Li sites in the Li layers and 25% for the Li site in the $LiSn_2$ layers). As such an end-member sample has no electrochemical interest, we did not pursue further studies here to survey whether these deviations could result from non-stoichiometry issues, extended defects or Li mobility.

As we increase the amount of Ru in Figure 1, the ^{7}Li spectra become broader, with components appearing at shifts as high as 500 ppm (see SI for deconvolution). These high shifts, well outside of the typical range for diamagnetic insulating solids, arise from the interaction of the nuclear spins with the unpaired electron spins. We study further the exact mechanism at the origin of these shifts to grasp further information on the detailed structure of the materials. A Knight shift (arising from conduction electrons) can be excluded as the EPR measurements did not detect any signal from conduction electrons.[13]

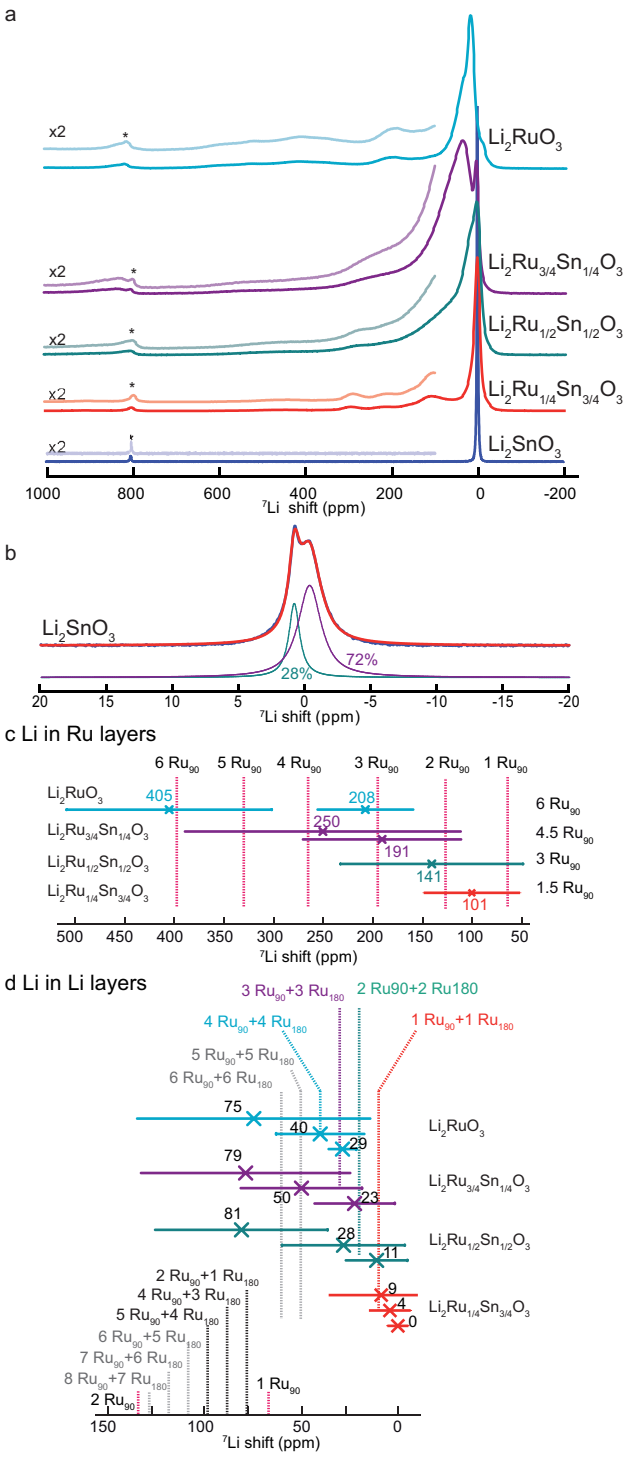

Figure 1. (a) ^{7}Li solid-state NMR spectra of the solid solution $Li_2Ru_{1-y}Sn_yO_3$ obtained at 4.7 T. Spinning sidebands are indicated with asterisks (MAS rate 62.5 kHz). (b) Decomposition of the spectrum of Li_2SnO_3, details in SI. (c, d) Main Li components in the Ru layers and in the Li layers respectively. The cross shows the position of the maximum intensity and the width of the bar indicates the full width at half height. The main shifts expected for a random substitution are shown in dotted coloured lines; other possibilities are in dotted black (Ru/Sn partial ordering) and grey (Ru/Li substitutions).

We account for the observed shifts in the NMR data of the family with the model for paramagnetic Fermi contact (FC) shifts developed by Grey et al.,[19] for lithium oxides containing paramagnetic metals with octahedral geometry. The authors demonstrated that the observed shifts can be interpreted using the sum of the individual contributions of all paramagnetic metal-O-Li bonds, each bond contributing to a positive or a negative shift depending on the metal-O-Li bond angle and the electronic configuration. As a consequence, the configurations of the cation coordination spheres around the lithium ions need to be considered for interpreting the ^{7}Li spectra, in terms of number and type of bonds to paramagnetic metals. The FC shift is expected to be dominant here, as the chemical shift range is negligible compared to the FC shift. Tin(IV) does not contribute to a FC shift in Li_2SnO_3 and hence in the whole $Li_xRu_{1-y}Sn_yO_3$ family, as its oxidation state remains unaltered.[13] The number of surrounding Ru and their position are therefore controlling the FC shift of the Li atoms.

For the $Li_2Ru_{1-y}Sn_yO_3$ materials, the Li are located in an oxygen octahedron surrounded by Li, Sn or Ru atoms: 12 atoms connected by 90° O-Li bonds are found in the first cation coordination sphere and 6 atoms are connected via 180° O-Li bonds in the second cation coordination sphere (Figure 2). Assuming a low-spin configuration as deduced from magnetic measurements, Grey's model indicates that the 90° Ru-O-Li bonds contribute to a positive FC shift (FC_{90}) through delocalization and the 180° Ru-O-Li bonds generate a negative FC shift (FC_{180}) on the Li by a polarization mechanism.

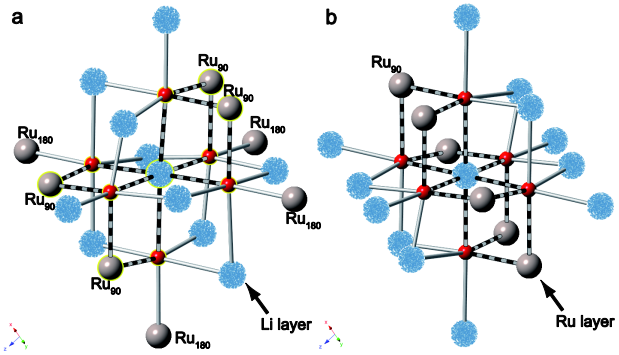

Figure 2. (a) Environment for Li in Li layers and (b) for Li in Ru layers in Li_2RuO_3. Ru are in shiny grey and Li are in blue, random fill. Oxygens (red) have a small diameter for easier reading of the figure. The Li-O-Ru bonds to consider for the central Li are shown with multiband cylinders. Note that each Ru_{90} creates two 90° bonds.

In the following paragraph, the structural differences that matter for the FC shift of the Li in the Ru layers (Li_{Li2Ru}) and in the Li layers (Li_{Li}) are detailed for Li_2RuO_3. The Li_{Li2Ru} (Figure 2b) are surrounded by 6 Ru_{90} atoms (honeycomb ordering) and no Ru_{180} in the second cation coordination sphere. These Li_{Li2Ru} should therefore display a shift of 12 FC_{90}, highly positive. On the other hand the coordination sphere of the Li_{Li} (Figure 2a) is composed of 4 Ru_{90} atoms and 4 Ru_{180} atoms (the 10 other sites being

Li). The resulting shift (8 FC_{90} + 4 FC_{180}) will be much smaller than for Li_{Li_2Ru}, as the 180° bonds contribute negatively. Based on the X-ray structure, we expect relative intensities of 25% and 75% for the Li_{Li_2Ru} and the Li_{Li} in Li_2RuO_3, respectively. Unfortunately the spectrum of Li_2RuO_3 does not display well-defined peaks as in Li_2MnO_3, indicating a deviation from the ideal structure. Stacking faults, as observed on Li_2MnO_3,[35] or distortions of the Ru network to form long and short Ru-Ru distances[36] could be at play.

For the mixed compounds, the chemical disorder introduced by Sn/Ru substitution needs to be taken into account. It is worth recalling the source of shifts and lineshapes before we interpret in detail the experimental spectra of the Sn/Ru substituted materials. In the present case the prevailing source of ^{7}Li shift is the FC shift mechanism arising from paramagnetic Ruthenium. Chemical disorder introduced by substitution of Ru by diamagnetic Sn has therefore the strongest effect. One peak is expected for each type of Ru configuration around the Li (number of Ru and type of Ru-O-Li bond) with an area controlled by its proportion in the material, while smaller variations induced by geometrical disorder (bond length, angle, etc…) result in the width of each component. NMR is well known for being a powerful tool to probe such disorder,[37] but its sensitivity to local environments is also a drawback when too many of those are present and/or have similar shifts. In that case, resolution is lost and the NMR peaks merge and appear as one average peak. The position of this peak then indicates the most populated environment(s), and its width is controlled by the number of merging peaks and their respective widths. Table S1 in SI indicates all the possible configurations around Li atoms. Twenty-two peaks are expected assuming only Ru/Sn and no Li/Ru substitution. Seven Ru configurations can be expected for Li_{Li_2Ru} (0 to 6 Ru_{90}). The range of possibilities (20) is larger for Li_{Li}, as Ru are present in the first and second coordination spheres (Ru_{90} and Ru_{180}).

Those configurations do not however happen with the same proportion in the crystal. Using the supercell programme,[33] the expected Li environments and their probability are surveyed *in the case of random substitution*. In $Li_2Ru_{0.25}Sn_{0.75}O_3$, nine non-negligible (>5% probability) environments are found for Li: Li surrounded by 0 Ru_{90} (5% from Li_{Li_2Ru}), 1 Ru_{90} (7% Li_{Li_2Ru} and 7% Li_{Li}) and 2 Ru_{90} (8% from Li_{Li_2Ru} and 7% from Li_{Li}), 1 Ru_{90} + 1 Ru_{180} (32% from Li_{Li}), 2 Ru_{90} + 1 Ru_{180} (9%; Li_{Li}), 1 Ru_{180} (7%; Li_{Li}) and 1 Ru_{90} + 2 Ru_{180} (5%; Li_{Li}). Note that the most probable environments is 1 Ru_{90} + 1 Ru_{180} for Li_{Li} and 1 or 2 Ru_{90} for Li_{Li_2Ru}, but that some environments can be present both in Li layers and in Ru layers, which complicates the interpretation.

The detailed prediction of the FC shifts need elaborate spin-polarized calculations[38,39] that go beyond the scope of this manuscript. However, based on Grey et al. model and the spectrum of $Li_2Ru_{0.25}Sn_{0.75}O_3$, we could determine the FC shift contributions FC_{90} and FC_{180} (on average +33 ppm and -56 ppm, as detailed in supplementary information). We consider these as average values, as FC_{180} was shown to be extremely dependent on the Ru-O-Li bond for a range of Ru(V) lithium oxides[40] and we do not expect the sensitivity to bond angle to be different for Ru(IV). Based on these values, we exploit the experimental spectra of the mixed Sn-Ru compounds. Table S1 in SI indicates the FC shifts calculated for the Li in all the possible Sn/Ru configurations, assuming no geometrical disorder.

Experimentally, the spectra become more shifted for increasing substitution of Sn by Ru, as expected for Li environments richer in Ru_{90}, but they also become less resolved due to an increased number of populated Ru configurations around the Li. Interestingly, the absence of major negative shift components in the ^{7}Li spectra of the whole family indicates that the Ru/Sn substitution results in general in a number of Ru_{90} higher than the number of Ru_{180}.

For a closer inspection of the paramagnetic part of the spectrum, a careful deconvolution was performed using the smallest necessary number of components (Figure S1). Valuable information on the Sn-Ru arrangement, which could not be accessed by other techniques, is obtained from the contribution of Li surrounded by only diamagnetic Sn and Li near 0 ppm. This contribution decreases with the amount of Sn in the sample as expected, but it is much higher than expected for a statistical substitution (7% for 25% Ru and 0.4% for 50% Ru). Furthermore, ^{119}Sn NMR experiments conducted on the same samples (Figure S2) detected a "Sn-only" signal more intense than expected and support this hypothesis. Note that no other phase was detected by X-rays.[13] The Ru substitution therefore creates preferentially "Sn-only", i.e. non-paramagnetic, lithium environments and consequently Ru-rich and Ru-poor environments in the material. Note that we do not know whether these environments are homogeneously distributed throughout the structure or whether they are "clustered" in the sample.

For the Ru-containing pristine materials, four main peaks were always found by deconvolution, accounting for ~20% of the signal each. In relatively good agreement with the expected shifts, the average FC shift increases experimentally with the Ru proportion. One peak is always much more shifted than the three others, and is assigned to the Li in Ru layers .Figure 1c shows the position and width at half-height of this high-shift peak, together with the shifts expected from the FC model (vertical lines) for a random substitution. Interestingly, the width of the Li_{2Ru} peak (the extension of the bar in figure 1c shows the width at half height) indicates that a non-negligible range of configurations with excess or missing Ru are created, in agreement with the previous observation. It is even more striking for Li_2RuO_3 and $Li_2Ru_{0.75}Sn_{0.25}O_3$, for which the high-shift range has to be described by two components (10% each). Part of it, but not all, might arise from a non-stoechiometry of the samples due to the volatility of Li during the synthesis. In the

case of high Ru content, the Ru propensity to "dimerize", as was observed in Li_2RuO_3, is most probably at stake.[36]

For Li_{Li} in Li layers, statistical substitution should result in one predominant environment for each composition (dotted coloured lines in Fig. 1d). Experimentally, the hypothesis of "Ru grouping" is further confirmed by the observation of three types of environments: the expected environment and environments slightly richer and slightly poorer in Ru. One of the Li_{Li} sites in the structure is distorted and might result in a slightly different FC shift, but this is not sufficient to explain the three other components in the spectrum. Many Ru configurations around the Li_{Li} are possible for a given number of Ru, and it is difficult to rationalize the observed shifts further in terms of numbers of Ru and more so Ru_{90} and Ru_{180}.

In the following we concentrate on the behaviour of the $Li_2Ru_{0.75}Sn_{0.25}O_3$ material (1-y=3/4, denoted hereafter Li_xRSO) that was shown to provide the best cycling performances of the family, using a combination of *ex situ* and *in situ operando* measurements. Resolution is low in NMR of such static solids due to the large anisotropic interactions. The solution is to pneumatically spin the sample, but spinning a battery is challenging due to eddy currents, heating, centrifugal forces and probe design issues. As a result, the high-resolution study is necessary *ex-situ*. Here we present the static *in situ* experiment together with the high-resolution *ex situ* study (with ultra-fast spinning for maximum resolution). We designed an electrochemical cell compatible with imaging, and we demonstrate its use with the characterization of $Li_2Ru_{0.75}Sn_{0.25}O_3$.

b) *Ex situ* characterization of cycled electrodes

When the $Li/Li_2Ru_{0.75}Sn_{0.25}O_3$ electrochemical cell is charged up to 4.6 V, two main steps appear: a sloping voltage from 3 V to 4 V and a plateau from 4 V to 4.6 V (Figure 3). The first one leads to a single phase ($Li_{1.3}Ru_{0.75}Sn_{0.25}O_3$) with Ru(V) and the latter to a peroxo/superoxo $Li_{0.5}Ru_{0.75}Sn_{0.25}O_3$ phase as previously determined by combined XPS and EPR measurements. However there is limited information on the Li removal process at the structural level. To get more insight into this issue, the ^7Li spectra of the partially oxidized electrodes (x_{Li}=1.3 and x=0.5) are shown in Figure 3. In all the samples a sharp peak is found in the diamagnetic region (~0 ppm), which we assign to diamagnetic species formed in the solid-electrolyte interface (SEI) and not completely removed from the material by the washing step. Note that the three spectra were scaled to have similar intensities but the intensity of the ^7Li spectrum for the $Li_{0.5}RSO$ is much lower (less Li atoms), resulting in an apparently more intense SEI peak.

As the sample is partially oxidized (Fig. 3, x_{Li}=1.3) we observe a surprising behavior. The ^7Li spectrum becomes broader and more symmetric, its shifts changes severely (183 ppm), and its intensity is much smaller than expected. Such behaviour was also revealed by a similar ^7Li spectrum (figure S3) for the isoelectronic $LiRu^VO_3$ phase, made electrochemically. We experienced difficulties spinning the rotor above 59 kHz, indicating increased electronic conductivity or magnetism. Two possible explanations can be put forward to account for the observed spectrum. One is nested in a reorganization of the Ru and Sn atoms, so that all the remaining Li (in both layers) have a similar environment. Another possibility is rooted in an increase of the metallic character of the sample following oxidation of the Ru, resulting in an average shift for all Li governed by the interaction with the itinerant electrons (as observed on $LiCoO_2$[41]).The second hypothesis is favoured, as it is consistent with the increased conductivity and EPR measurement which indicated a partial localization but strong electron mobility at room temperature.[13]

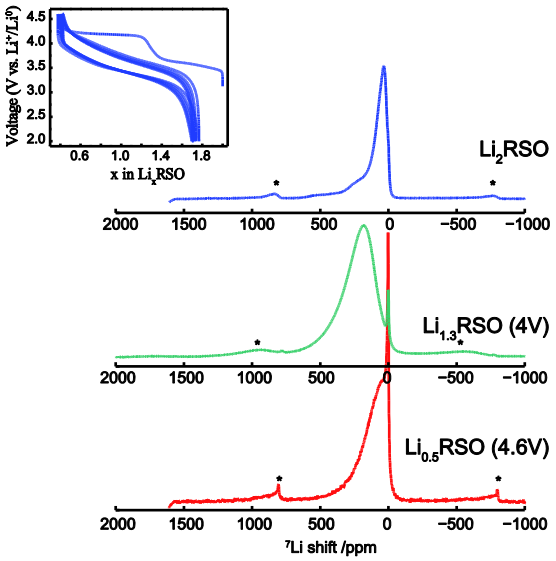

Figure 3. ^7Li solid-state NMR spectra in the first charge of $Li_2Ru_{0.75}Sn_{0.25}O_3$ scaled to have the same intensity. Spinning sidebands are indicated with asterisks (MAS rate 62.5 kHz except for $Li_{1.3}RSO$: 59 kHz). The sharp peaks near 0 ppm in the cycled materials arise from diamagnetic species formed in the solid-electrolyte interface.

When the sample is further oxidized to 4.6 V (x_{Li}=0.5), the main peak shifts back to the 60 ppm-region, close to the pristine material, with a tail towards higher shifts. Absolute interpretation of the shift needs new models for the system considering the position and electronic structure of Ru and O during cycling. One possibility is the change in the electronic environment experienced by Li with the formation of peroxo/superoxo-like species during oxidation. Nonetheless, the non-gaussian shape and wider ^7Li spectrum of the $Li_{0.5}RSO$ sample compared to the pristine indicate a large disorder in the system caused by electrochemical (possibly mixed Ru oxidation state), chemical (Sn/Ru/Li redistribution) and/or geometrical (bonds, angles) modifications, that introduces more components in the NMR spectrum. Chemical disordering in the structure was also observed in recent STEM studies on similar $Li_2Ru_{1-y}Ti_yO_3$ and Li_2RuO_3 systems.[42]

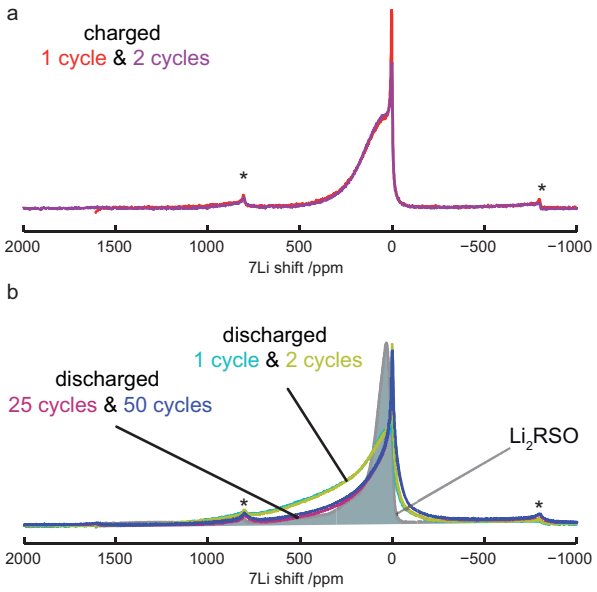

Figure 4. ^{7}Li solid-state NMR spectra of multiple charge-discharge cycles of $Li_2Ruo.75Sn_{0.25}O_3$ (a) Spectra of the charged electrode in 1st and 2nd cyles. (b) Spectra of discharged electrodes in the 1st, 2nd, 25th and 50th cycles, compared to the pristine electrode (full). The sharp components near 0 ppm in the cycled materials arise from diamagnetic species formed in the solid-electrolyte interface. Spinning sidebands are indicated with asterisks (MAS rate 62.5 kHz).

The evolution of the ^{7}Li spectrum was also monitored upon further cycling. In Figure 4a, the ^{7}Li spectra for charged samples obtained from two different batteries, cycled once (red) or twice (purple), are superimposed. The spectra are identical, with the exception of the diamagnetic Li signal arising from SEI, expected to vary from battery to battery. This observation further confirms the reproducibility of the material detected from the electrochemical studies. We collected additionally the ^{7}Li spectra for samples in the discharged state after 1, 2, 25 and 50 cycles. The spectra of the discharged materials after 1 and 2 cycles neatly superimpose (Fig. 4b), but the more intense tail compared to the pristine Li_2RSO sample in the high-shift range (Ru_{90}-rich environments) suggests that a grouping of the Ru is triggered in the initial cycling and is not completely recovered upon a full cycle, in agreement with previous XRD measurements.

The evolution of that tail with the number of cycles indicates that this grouping of the Ru in the Ru layers is reduced until the 25th cycle (or that Li atoms do not return close to these environments). This is at first surprising, although one could envision that a few cycles are necessary to free atom migration (e.g. remove pinning defects) within the structure and therefore facilitate their return to their nearly original states. Purely coincidentally or not, such a behavior mirrors the capacity retention of similar electrodes which decay till 25 cycles prior to stabilization, hence indicating a possible correlation between capacity decay and Ru/Sn organization in the metal layer during the first cycles. It is worth mentioning the absence of further evolution of the ^{7}Li spectra by extending the cycling till 50 cycles (Fig. 4b), highlighting once more the exceptional cyclability of the $Li_xRu_{0.75}Sn_{0.25}O_3$ family of compounds.

The ex-*situ* measurements were successful in spotting the local chemical disorder triggered by the removal and uptake of Li, and they could indicate an increase in the "grouping" of the Ru atoms in the Ru layers during the first cycles, followed by a small decrease of this "grouping" at the end of the formation cycles. Additionally, a surprising behavior was observed at 4 V with an increase in metallicity and at 4.6 V with a spectrum closer to the pristine/fully reduced electrode. In order to shed more light on this issue and to get better time and voltage resolution without any risk of evolution during battery disassembly, we complemented our study with real-time observations.

Next, our new electrochemical cell and probe design are presented, then we demonstrate how the combination of imaging and spectroscopy enhances the understanding of the spectra and finally we focus on the time-resolved information we gather for $Li_xRu_{0.75}Sn_{0.25}O_3$ in the first two cyles, especially at half charge.

c) *Operando* cell and probe design

In situ NMR brings special constraints on the cell design. Stainless steel containers cannot be used as they prevent acquisition of the NMR signal of the components inside the battery. Two types of electrochemical cell design for *in situ* NMR, compatible with standard NMR probes, have been proposed previously: flexible plastic pouch cells[28,29,31] and a cylindrical polypropylene cell.[30] Polarization studies on liquid electrolytes have also been performed inside a liquid-state NMR tube.[43–45] Our new cylindrical design, similar to a "Swagelok" cell, as shown in Figure 5, ensures control on the compression in the active cell part.

Contrary to Poli et al.,[30] the cell is positioned vertically in a Bruker *diff*50 probe equipped with a saddle coil. As a result, the two current collectors are horizontal in the magnet, which is better adapted to the geometry of the radio-frequency field created in the saddle coil and ensures maximal RF-field penetration in the electrochemical cell.[46] The other advantage of such a configuration is the cylindrical symmetry along the vertical axis. The large magnetic field gradient available along the vertical axis in the *diff*50 probe allows performing chemical shift imaging (CSI)[47], a combination of 1D imaging and spectroscopy. The formation of dendrites and mossy lithium by polarizing symmetric Li pouch cells was followed by CSI,[48] with a 3D gradient NMR/MRI probe. Thanks to the cylindrical symmetry of our new design and its vertical positioning inside the probe, meaningful results can be obtained here with a 1D image (projection) along the vertical axis. This extends the range of probes suitable for CSI imaging (only one z-gradient needed).

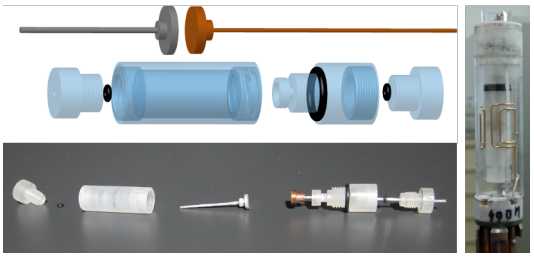

Figure 5. Electrochemical cell

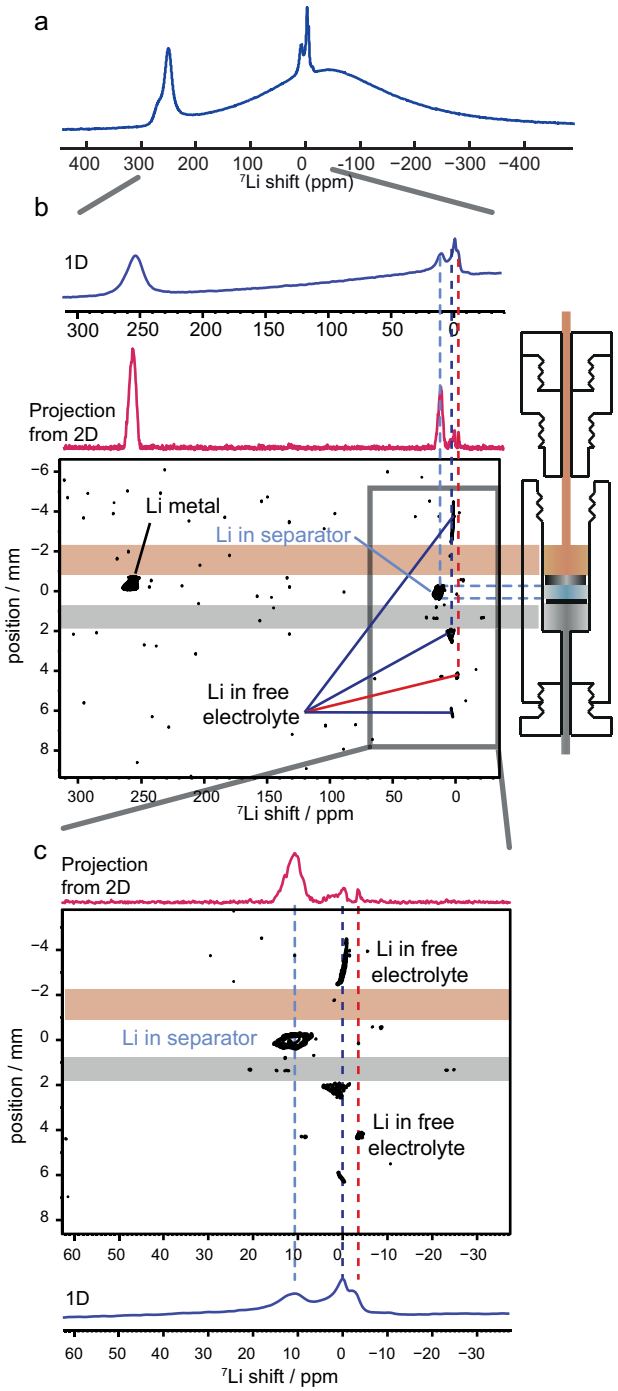

Figure 6. (a) Spectrum of the electrochemical cell containing the half-cell $Li_2Ru_{0.75}Sn_{0.25}O_3$//Li with LP30 electrolyte, (b) chemical shift imaging of the cell, (c) zoom in the electrolyte part.

Electrochemically-wise, the validity of this new cell design is proved by the voltage-composition profile of the $Li/Li_2Ru_{0.75}Sn_{0.25}O_3$ cell, which is identical to the profile obtained in cycling classical swageloks or coin cells over a few cycles (see below).

d) *In situ* and *operando* characterization of Li_xRSO

An *operando* NMR characterization of Li_xRSO is performed with our electrochemical cell, bearing in mind that resolution is poorer in a static mode and that magnetic susceptibility variations caused by heterogeneities in the battery shifts the peaks.[49,50] O*perando* measurements have however the great advantage of measuring a series of spectra on the same battery, and they give a much better time/voltage-resolved picture of the phenomena at stake. In our case the signal to noise was good enough to measure one spectrum in 30 min and provided 240 spectra per electrochemical cycle.

Figure 6a shows the ^7Li spectrum (Hahn echo) of the cell placed onto the NMR probe, just after assembly in the glovebox and before any cycling. The three Li-based components of the cell (lithium negative electrode, electrolyte and positive electrode) are observed in the ^7Li NMR spectrum. The sheet of metallic lithium is Knight-shifted to 258 ppm. The electrolyte peaks appear as several narrow peaks in the diamagnetic region (11, 0, -3 ppm), due to variations of the magnetic susceptibility in different parts of the cell. They are identified with the chemical imaging technique in the next paragraph. Finally, the pristine electrode is the broad component centered at -5 ppm, with a component towards higher shifts. This shift is quite different from the maximum component in the *ex situ* Li_2RSO spectrum (centered at +28.5 ppm), most probably due to temperature effects and anisotropic magnetic susceptibility of the film.

Chemical shift imaging is a very powerful way to obtain localized spectra, e.g. spectra of portions of the sample. With this other method we identify the position of the lithium metal and of the electrolyte that give rise to the three peaks. The resulting image/spectrum of the $Li/Li_2Ru_{0.75}Sn_{0.25}O_3$ cell, shown in Figure 6b, correlates the spectrum (horizontally) with the 1D position (vertical). We used the vertical magnetic field gradient available in this probe to select horizontal slices of the electrochemical cell; its cylindrical symmetry ensures that a 1D image is sufficient. We detect in Figure 6b the Li metal at the top of the cell, with a skin-depth effect reducing the signal at the center of the foil. The image-spectrum correlation is useful to assign the electrolyte peaks (zoom in Figure 6c). The broadest peak (11 ppm), at the centre of the cell, is the electrolyte adsorbed in the separator. The 0 ppm peak is free electrolyte trapped by the O-rings during assembly along the current collector wires (mostly the top copper wire). The -3 ppm peak is further away and arises from a drop of electrolyte trapped at the bottom of the cell. Unfortunately the broad electrode signal cannot be imaged with the present technique because its transversal relaxation time is too short for the signal to survive the series of radiofrequency and gradient pulses required

for imaging. This is a well-known but not trivial issue in imaging and work is in progress to address it.

Figure 7 shows the series of ^{7}Li spectra acquired during the first charge of the Li/$Li_2Ru_{0.75}Sn_{0.25}O_3$ cell with in Figure 7d the characteristic increase in signal for metallic lithium deposition. The shift of the deposited lithium is slightly higher than that of the Li sheet due to its mossy/dendritic morphology.[51] It could be surprising to note that, as the voltage becomes greater than 4 V, the Li signal does not increase anymore. Grey et al. observed a similar effect and explained it in terms of a skin-depth limitation,[51] associated with a smoother/thicker metallic Li deposition.

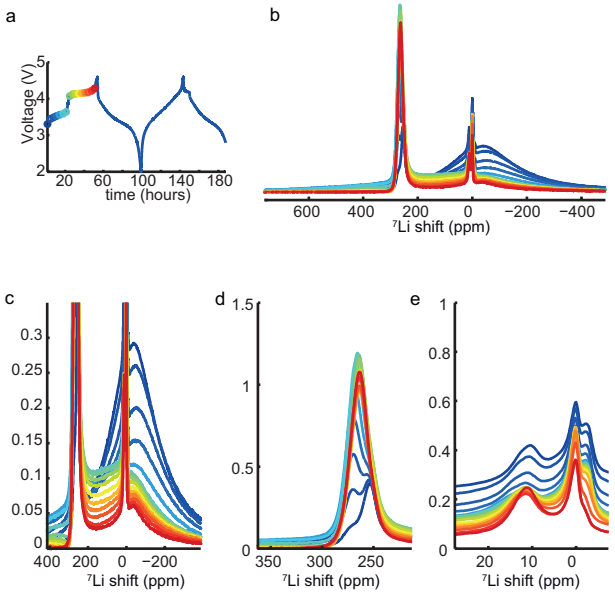

Figure 7. Operando ^{7}Li NMR spectra for the first charge of the Li_xRSO half-cell: (a) electrochemical profile, (b) full spectra, (c) positive electrode region, (d) metallic Li region and (e) electrolyte peaks. The spectra are color-coded to indicate the corresponding electrochemical state.

The evolution of the NMR peaks associated to the electrolyte when the cell is charged is also followed in real time (Fig. 7e). Although we cannot be fully quantitative because the NMR signal of the electrolyte is not fully relaxed (short recycling delay), the absence of striking changes in the signal indicates that no significant electrolyte decomposition occurs during these experiments. Note that the evolution of the base line is not related to the electrolyte but to the modifications of the broad overlapping peak of the positive electrode. Keeping this effect in mind, one observed feature is the slight displacement towards higher shifts of the peak associated to the electrolyte adsorbed in the separator (11 ppm). This evolution mirrors that of the Li metal, while the intensities of these two peaks vary inversely. We assign these effects to both magnetic susceptibility or conductivity changes in the metallic Li sheet (its surface) that influence in turn the electrolyte in contact. We also observed small reversible variations in the minor electrolyte peaks (at 0 and -3 ppm, Fig. 7e) upon cycling. Further work is in progress to identify the origin of these variations.

Lastly, in Figure 7c, we report the evolution of the broad ^{7}Li spectra for the Li_xRSO electrode during its charge, with a continuous broadening and decrease of the signal as Li atoms are deintercalated from the material. As the cell voltage approaches 4 V (e.g. jump on the voltage curve), we note a clear displacement of the peak towards higher shifts, that confirms the *ex situ* measurements. As the voltage is further increased, the signal becomes less intense and moves back to lower shifts, so that at 4.6 V the peak has a position similar to that of the pristine spectrum but much broader, in agreement with the *ex situ* observations.

Next we exploit the series of spectra collected through these *operando* NMR measurements in an attempt to get further insight on the mechanistic of the Li removal-uptake process. Figure 8 shows the static *in situ* ^{7}Li spectrum at points of interest in the first charge. A clean deconvolution of the *operando* spectra is difficult to perform as the lineshapes are not Gaussian (the distribution of shifts is not random) and more than 15 components would be needed, resulting in a highly under-determined fit., However, our operando data become very informative by comparing the *ex situ* and *in situ* spectra. For instance, we aligned the maximum of the signal in the *ex situ* MAS spectrum of the pristine material with its counterpart in the *in situ* static spectrum to compensate for the temperature and magnetic susceptibility effects. The same shift was then applied to all the MAS spectra. After this treatment, the collected *in situ* spectrum at 4 V and 4.6 V are in perfect agreement with the *ex situ* data collected on the $Li_{1.3}RSO$ and $Li_{0.6}RSO$ samples. This observation not only validates our *in situ* experiment, but more importantly indicates that all the phenomena (Li environment changes, increased disorder) observed so far are definitely occurring during cycling, not after cell relaxation. In these selected slices, the second cycle shows differences with the first cycle, as expected. The *operando* spectra are exploited in a more detailed manner in the next paragraph.

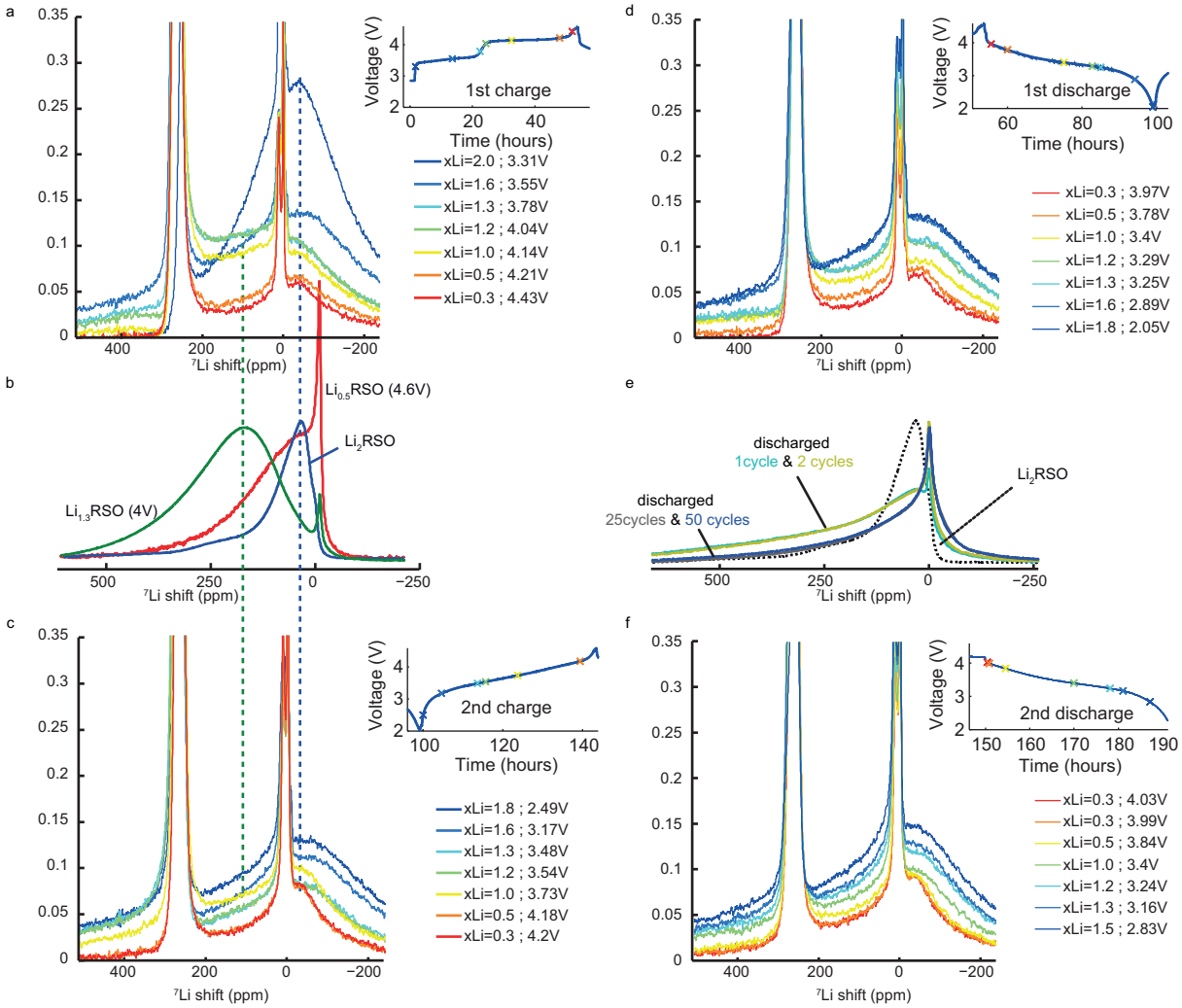

Figure 8. *Operando* first (a) and second (c) charge ^{7}Li NMR spectra compared with *ex situ* MAS ^{7}Li spectra (b, e). First (d) and second (f) discharge *operando* spectra. Insets in (a), (c), (d) and (f) indicate the electrochemical status for each spectra (color-coded). The incertitude in the value of x_{Li} (amount of Li per $Ru_{0.75}Sn_{0.25}$ unit) is ±0.1 due to the initial irreversibility of 0.2.

Figure 9 shows the time/voltage resolution that is obtainable through *operando* NMR. As the spectra cannot be deconvoluted reliably, the intensity of the *in situ* spectrum is plotted versus the amount of Li in the positive electrode for two NMR shifts (-40 ppm and 112 ppm), chosen to coincide with the position of the maxima of the *ex situ* spectra before any charge (pristine) and at 4V in the first cycle respectively. The -40 ppm region (Fig. 9a) decreases dramatically at the very beginning of the 1st charge (red circles), partly due to the removal of Li but also due to a broadening of this component. The number of accessible Ru configurations and oxidation states is indeed increased around the Li. The spectrum in this area does not display any remarkable evolution in the remaining of the charge; it simply decreases as more Li are removed. The 110 ppm region (Fig. 9d) on the other hand shows clearly a maximum corresponding to the jump in voltage (x_{Li}=1.3, 3.9V) in the first charge. This is in good agreement with our *ex situ* NMR data at 4V.

The first discharge is clearly different in the 110 ppm range for x_{Li} higher than 0.8 (Fig 9d). No clear contribution of a phase with increased metallicity is detected in this first discharge. The initial spectrum intensity is never fully recovered due to the broadening of the spectrum. Chemical and geometrical disorder are induced by the delithiation-lithiation process and result in a smoother spectrum.

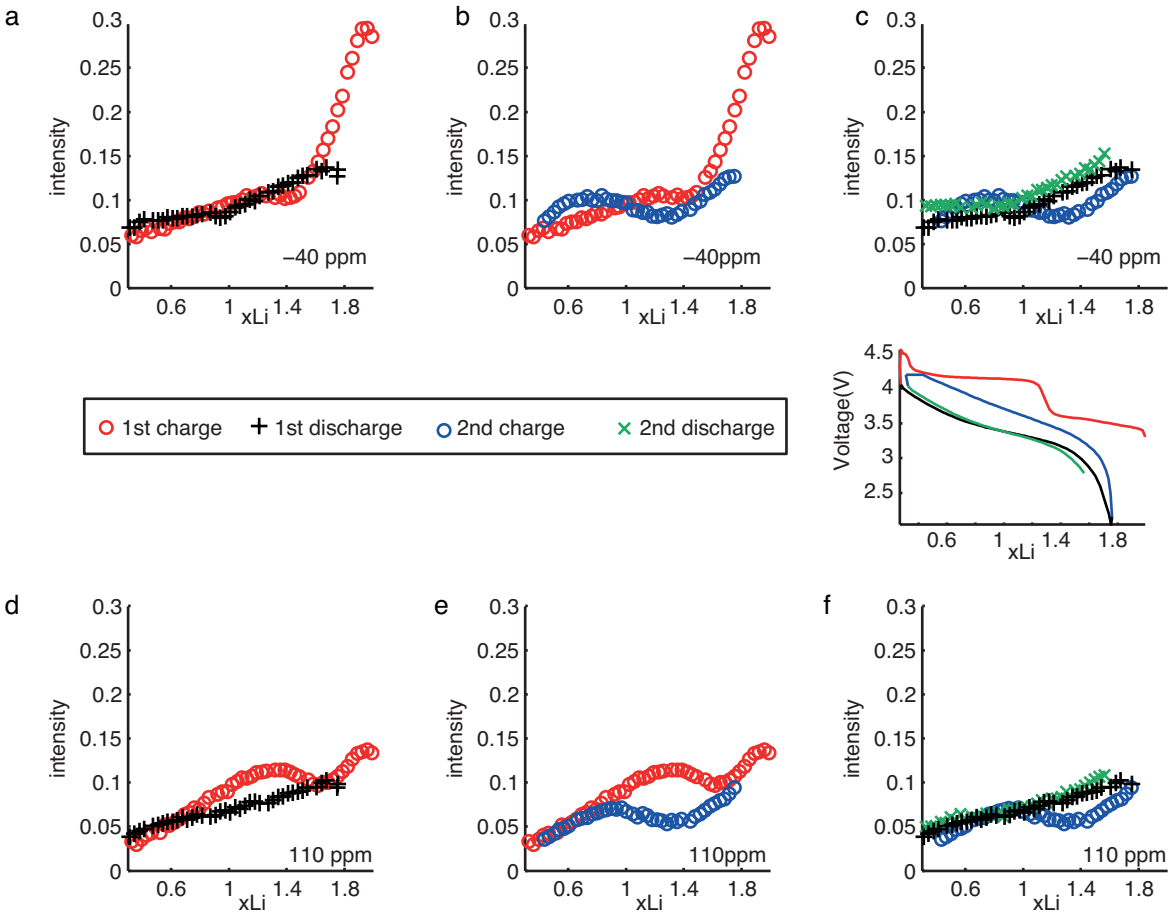

Figure 9. Variations of intensity in two regions of interest of the ^{7}Li spectra for charge (circle) and discharge (cross), in the 1st (red) and 2nd (blue) cycles.

The second charge is different from the first charge and discharge in Figure 9b and 9e, as expected with a material altered compared to the pristine material. A striking difference is observed in both regions of the NMR spectrum. While in the 1st charge, the 110 ppm region displayed a maximum in intensity for x_{Li}=1.3, the maximum in intensity is now observed for x_{Li}=0.7. In addition this effect is more intense in the -40 ppm region than in the 110 ppm region, unlike the first charge. This signature differ from the first charge and indicates that the pathway in the second charge is different from the first charge, in good agreement with the electrochemical curve. The peaks are first broadening as the first half of the lithium atoms are removed (2>x_{Li}>1.3). In the second part of the charge, a new environment is created at a smaller FC shift. Although different from the first charge, this environment occurs around 4 V, in the same range as the phase with increased metallicity of the first charge

Finally, the spectra on first and second discharge superimpose almost completely in Figure 9c and 9f, indicating that a stationary regime is obtained for the discharge very quickly. The intensity, almost linearly dependent on the lithiation degree, indicates a smooth intercalation of Li. Interestingly, the difference between the second charge and the following discharge indicates that the pathways on charge and discharge are still different after the first cycle, even though the discharges are smooth. Such a difference is most likely related to a slight difference in the kinetics of the Li-driven structural modifications on charge and on discharge.

Conclusions

As a conclusion, NMR is extremely sensitive to local defects and here the complexity of the material hinders the analysis, namely (i) substitutional Sn/Ru disorder, (ii) the tendency of Ru to dimerize and (iii) potentially stoichiometric issues. However a non-random substitution of the Ru by Sn in the $Li_2Ru_{1-y}Sn_yO_3$ family, not detected with standard characterization tools such as X-ray diffraction, is observed by *ex-situ* ^{7}Li and ^{119}Sn NMR and indicates Ru-rich and Ru-poor environments in the material.

A new cell design is also presented which allows excellent electrochemical cycling for operando ^{7}Li NMR. *Ex situ* MAS NMR experiments are extremely complementary to *in situ operando NMR* measurements, especially when chemical disorder and overlapping peaks create

non-gaussian lineshapes. Assignment of the shifts is made possible by *ex situ* extremely fast MAS *NMR* and it can be transferred for interpretation of the *operando* static NMR measurement, which brings much better time/voltage resolution. In addition, chemical shift imaging is used to identify the source and z-position of the three electrolyte signals in the electrochemical cell.

On the material side, a non-random substitution of Sn and Ru in the $Li_2Ru_{1-y}Sn_yO_3$ family is detected. The exceptional reproducibility upon cycling of this material is also clearly confirmed in this combined *ex situ*/*in situ operando* study. Upon cycling $Li_2Ru_{0.75}Sn_{0.25}O_3$, a very different NMR signature is found for the lithium atoms in the 1st charge at x_{Li}=1.3, which is validated by *in situ operando* measurements. We hypothesize that it is caused by an increased metallicity of the sample and possibly a Ru-Sn reorganisation in the metal layers during charge, resulting in a higher extent of (or more distributed) chemical disorder after one cycle. The pathways are similar for all discharges, indicating a smooth reintercalation. As expected from the electrochemical curve, the pathway taken on 2nd charge is different from the first. We detect however that a difference in pathways remains between the charges and discharges, even after the first cycle.

Finally we observe with both *in situ operando* and *ex situ* NMR that the average FC shift and distribution of FC shifts for the remaining Li in the 4.6 V phase ($Li_{0.5}Ru_{0.75}Sn_{0.25}O_3$) are not strikingly different from the $Li_2Ru_{0.75}^{IV}Sn_{0.25}O_3$ phase. This is somehow intriguing as we expect a reductive coupling mechanism at full lithiation to change the electronic structure and to distort the geometry of the structure significantly, hence modifying the ^{7}Li FC shift. A part of the puzzle remains and new models need to be developed and refined on model compounds with less sources of disorder. This definitely stands as a challenge to the community since this generation of high capacity electrodes enlisting both cationic and anionic redox processes are quickly developing.

ASSOCIATED CONTENT

Supporting Information. ^{7}Li and ^{119}Sn NMR spectra of the pristine family. Deconvolution of the ^{7}Li spectra and details on the determination of the FC_{90} and FC_{180} contributions. Predicted FC shifts for all types of Li environments. *Ex situ* ^{7}Li spectra for the first charge of Li_2RuO_3. Video of the evolution of in situ and operando NMR of $Li_2Ru_{0.75}Sn_{0.25}O_3$. "This material is available free of charge via the Internet at http://pubs.acs.org."

AUTHOR INFORMATION

Corresponding Author

*elodie.salager@cnrs-orleans.fr

Present Addresses

ZhongLi Wang: National High Field Laboratory, Florida State University, 1800 E. Paul Dirac Dr., Tallahassee, FL 32310-3706.

Author Contributions

ZW, PM, MD, VSK and ES conceived the first prototype of the electrochemical cell. JBM, MS and JMT upgraded that prototype for the experiments presented here. MS and JMT made the pristine materials and the electrochemical cycling for the *ex situ* samples. ES, VSK, MS and MT acquired the NMR experiments. All authors discussed the results.

Funding Sources

The authors acknowledge support from the CNRS, from the Agence Nationale de la Recherche (ANR) with the LABEX STORE-EX (ANR-10-LABX-76) and the grant MILIFOX (ANR-09-BLAN-0188) and from the European Commission through the European Regional Development Fund (ERDF/FEDER) in region Centre.

ACKNOWLEDGMENT

We thank S. Cadars and K. Okhotnikov (CEMHTI) for their program "supercell"; E Raymundo-Pinero (CEMHTI) for her VSP galavanostat; E. Veron (CEMHTI) for X-ray characterization; F. Fayon, P. Florian, D. Massiot (CEMHTI) for valuable discussion on fitting. We also thank F. Poli (CRMD, Orleans), M. Ménétrier (ICMCB, Bordeaux) and C.P. Grey (U. Cambridge) for valuable discussions on *in situ* cells, M.L. Doublet (ICG, Montpellier) for helpful discussions on her calculations on this family,[13] G. Rousse (UPMC, Paris) for squid measurements and K. Ramesha (CSIR, India) for providing some of the samples.

ABBREVIATIONS

NMR, nuclear magnetic resonance; MAS, magic angle spinning; FC, Fermi contact; Li_xRSO, $Li_xRu_{0.75}Sn_{0.25}O_3$; MRI, magnetic resonance imaging; CSI, chemical shift imaging

REFERENCES

(1) Mizushima, K.; Jones, P. C.; Wiseman, P. J.; Goodenough, J. B. *Mater. Res. Bull.* **1980**, *15*, 783–789.
(2) Ohzuku, T.; Makimura, Y. *Chem. Lett.* **2001**, 642–643.
(3) Lu, Z.; MacNeil, D. D.; Dahn, J. R. *Electrochem. Solid-State Lett.* **2001**, *4*, A200–A203.
(4) Ellis, B. L.; Lee, K. T.; Nazar, L. F. *Chem. Mater.* **2010**, *22*, 691–714.
(5) Kraytsberg, A.; Ein-Eli, Y. *Adv. Energy Mater.* **2012**, *2*, 922–939.
(6) Hu, M.; Pang, X.; Zhou, Z. *J. Power Sources* **2013**, *237*, 229–242.
(7) Lu, Z.; MacNeil, D. D.; Dahn, J. R. *Electrochem. Solid-State Lett.* **2001**, *4*, A191–A194.
(8) Johnson, C. S.; Kim, J.-S.; Lefief, C.; Li, N.; Vaughey, J. T.; Thackeray, M. M. *Electrochem. Commun.* **2004**, *6*, 1085–1091.
(9) Park, Y. J.; Hong, Y.-S.; Wu, X.; Ryu, K. S.; Chang, S. H. *J. Power Sources* **2004**, *129*, 288–295.
(10) Bareño, J.; Balasubramanian, M.; Kang, S. H.; Wen, J. G.; Lei, C. H.; Pol, S. V.; Petrov, I.; Abraham, D. P. *Chem. Mater.* **2011**, *23*, 2039–2050.
(11) Jarvis, K. A.; Deng, Z.; Allard, L. F.; Manthiram, A.; Ferreira, P. J. *J. Mater. Chem.* **2012**, *22*, 11550–11555.
(12) Sathiya, M.; Ramesha, K.; Rousse, G.; Foix, D.; Gonbeau, D.; Prakash, A. S.; Doublet, M. L.; Hemalatha, K.; Tarascon, J.-M. *Chem. Mater.* **2013**, *25*, 1121–1131.
(13) Sathiya, M.; Rousse, G.; Ramesha, K.; Laisa, C. P.; Vezin, H.; Sougrati, M. T.; Doublet, M.-L.; Foix, D.; Gonbeau, D.; Walker, W.; Prakash, A. S.; Ben Hassine, M.; Dupont, L.; Taras-

con, J.-M. *Nat. Mater.* **2013**, *12*, 827–835.
(14) Hodeau, J.; Marezio, M.; Santoro, A.; Roth, R. *J. Solid State Chem.* **1982**, *45*, 170–179.
(15) James, A.; Goodenough, J. *J. Solid State Chem.* **1988**, *74*, 287–294.
(16) Kobayashi, H.; Kanno, R.; Kawamoto, Y.; Tabuchi, M.; Nakamura, O.; Takano, M. *Solid State Ion.* **1995**, *82*, 25–31.
(17) Mustarelli, P.; Massarotti, V.; Bini, M.; Capsoni, D. *Phys. Rev. B* **1997**, *55*, 12018.
(18) Paik, Y.; Grey, C. P.; Johnson, C. S.; Kim, J.-S.; Thackeray, M. M. *Chem. Mater.* **2002**, *14*, 5109–5115.
(19) Grey, C. P.; Dupré, N. *Chem. Rev.* **2004**, *104*, 4493–4512.
(20) Cahill, L. S.; Yin, S.-C.; Samoson, A.; Heinmaa, I.; Nazar, L. F.; Goward, G. R. *Chem. Mater.* **2005**, *17*, 6560–6566.
(21) Jiang, M.; Key, B.; Meng, Y. S.; Grey, C. P. *Chem. Mater.* **2009**, *21*, 2733–2745.
(22) Koga, H.; Croguennec, L.; Mannessiez, P.; Ménétrier, M.; Weill, F.; Bourgeois, L.; Duttine, M.; Suard, E.; Delmas, C. *J. Phys. Chem. C* **2012**, *116*, 13497–13506.
(23) Alexander, A.; Battle, P. D.; Burley, J. C.; Gallon, D. J.; Grey, C. P. *J. Mater. Chem.* **2003**, *13*, 2612–2616.
(24) Battle, P. D.; Grey, C. P.; Hervieu, M.; Martin, C.; Moore, C. A.; Paik, Y. *J. Solid State Chem.* **2003**, *175*, 20–26.
(25) Rodgers, J. A.; Battle, P. D.; Dupré, N.; Grey, C. P.; Sloan, J. *Chem. Mater.* **2004**, *16*, 4257–4266.
(26) Rodgers, J. A.; Battle, P. D.; Grey, C. P.; Sloan, J. *Chem. Mater.* **2005**, *17*, 4362–4373.
(27) Gerald II, R. E.; Sanchez, J.; Johnson, C. S.; Klingler, R. J.; Rathke, J. W. *J. Phys. Condens. Matter* **2001**, *13*, 8269.
(28) Chevallier, F.; Letellier, M.; Morcrette, M.; Tarascon, J.-M.; Frackowiak, E.; Rouzaud, J.-N.; Béguin, F. *Electrochem. Solid-State Lett.* **2003**, *6*, A225.
(29) Key, B.; Bhattacharyya, R.; Morcrette, M.; Seznéc, V.; Tarascon, J.-M.; Grey, C. P. *J. Am. Chem. Soc.* **2009**, *131*, 9239–9249.
(30) Poli, F.; Kshetrimayum, J. S.; Monconduit, L.; Letellier, M. *Electrochem. Commun.* **2011**, *13*, 1293–1295.
(31) Shimoda, K.; Murakami, M.; Takamatsu, D.; Arai, H.; Uchimoto, Y.; Ogumi, Z. *Electrochimica Acta* **2013**, *108*, 343–349.
(32) Massiot, D.; Fayon, F.; Capron, M.; King, I.; Le Calvé, S.; Alonso, B.; Durand, J.-O.; Bujoli, B.; Gan, Z.; Hoatson, G. *Magn. Reson. Chem.* **2002**, *40*, 70–76.
(33) Okhotnikov, K.; Cadars, S. *manuscript in preparation*.
(34) Teo, L. P.; Buraidah, M. H.; Nor, A. F. M.; Majid, S. R. *Ionics* **2012**, *18*, 655–665.
(35) Bréger, J.; Jiang, M.; Dupré, N.; Meng, Y. S.; Shao-Horn, Y.; Ceder, G.; Grey, C. P. *J. Solid State Chem.* **2005**, *178*, 2575–2585.
(36) Miura, Y.; Yasui, Y.; Sato, M.; Igawa, N.; Kakurai, K. *J. Phys. Soc. Jpn.* **2007**, *76*, 033705.
(37) Massiot, D.; Messinger, R. J.; Cadars, S.; Deschamps, M.; Montouillout, V.; Pellerin, N.; Veron, E.; Allix, M.; Florian, P.; Fayon, F. *Acc. Chem. Res.* **2013**, *46*, 1975–1984.
(38) Carlier, D.; Ménétrier, M.; Grey, C. P.; Delmas, C.; Ceder, G. *Phys. Rev. B* **2003**, *67*, 174103.
(39) Middlemiss, D. S.; Ilott, A. J.; Clément, R. J.; Strobridge, F. C.; Grey, C. P. *Chem. Mater.* **2013**, *25*, 1723–1734.
(40) Battle, P. D.; Grey, C. P.; Rodgers, J. A.; Sloan, J. *Solid State Sci.* **2006**, *8*, 280–288.
(41) Ménétrier, M.; Saadoune, I.; Levasseur, S.; Delmas, C. *J. Mater. Chem.* **1999**, *9*, 1135–1140.
(42) Sathiya, M.; et. al. *submitted*.
(43) Hallberg, F.; Furó, I.; Yushmanov, P. V.; Stilbs, P. *J. Magn. Reson.* **2008**, *192*, 69–77.
(44) Klett, M.; Giesecke, M.; Nyman, A.; Hallberg, F.; Lindström, R. W.; Lindbergh, G.; Furó, I. *J. Am. Chem. Soc.* **2012**, *134*, 14654–14657.
(45) Krachkovskiy, S. A.; Pauric, A. D.; Halalay, I. C.; Goward, G. R. *J. Phys. Chem. Lett.* **2013**, *4*, 3940–3944.
(46) Ilott, A. J.; Chandrashekar, S.; Klöckner, A.; Chang, H. J.; Trease, N. M.; Grey, C. P.; Greengard, L.; Jerschow, A. *J. Magn. Reson.* **2014**, *245*, 143–149.
(47) Callaghan, P. T. *Principles of Nuclear Magnetic Resonance Microscopy*; Oxford University Press, 2003.
(48) Chandrashekar, S.; Trease, N. M.; Chang, H. J.; Du, L.-S.; Grey, C. P.; Jerschow, A. *Nat. Mater.* **2012**, *11*, 311–315.
(49) Trease, N. M.; Zhou, L.; Chang, H. J.; Zhu, B. Y.; Grey, C. P. *Solid State Nucl. Magn. Reson.* **2012**, *42*, 62–70.
(50) Zhou, L.; Leskes, M.; Ilott, A. J.; Trease, N. M.; Grey, C. P. *J. Magn. Reson.* **2013**, *234*, 44–57.
(51) Bhattacharyya, R.; Key, B.; Chen, H.; Best, A. S.; Hollenkamp, A. F.; Grey, C. P. *Nat. Mater.* **2010**, *9*, 504–510.

SYNOPSIS TOC